NeuroImage 65 (2013) 529–539

Contents lists available at SciVerse ScienceDirect

NeuroImage

journal homepage: www.elsevier.com/locate/ynimg

Epoch-specific functional networks involved in working memory

Todd S. Woodward [a,b,*], Eva Feredoes [c], Paul D. Metzak [a,b], Yoshio Takane [d], Dara S. Manoach [e,f,g]

[a] Department of Psychiatry, University of British Columbia, Vancouver, BC, Canada
[b] BC Mental Health and Addictions Research Institute, Vancouver, BC, Canada
[c] School of Psychology and Clinical Language Sciences, University of Reading, Reading, UK.
[d] Department of Psychology, McGill University, Montreal, PQ, Canada
[e] Department of Psychiatry, Massachusetts General Hospital, Charlestown, MA 02129, USA
[f] Athinoula A. Martinos Center for Biomedical Imaging, Charlestown, MA 02129, USA
[g] Harvard Medical School, Boston, MA 02215, USA

ARTICLE INFO

Article history:
Accepted 28 September 2012
Available online 4 October 2012

ABSTRACT

Working memory (WM) is not a unitary construct. There are distinct processes involved in encoding information, maintaining it on-line, and using it to guide responses. The anatomical configurations of these processes are more accurately analyzed as functionally connected networks than collections of individual regions. In the current study we analyzed event-related functional magnetic resonance imaging (fMRI) data from a Sternberg Item Recognition Paradigm WM task using a multivariate analysis method that allowed the linking of functional networks to temporally-separated WM epochs. The length of the delay epochs was varied to optimize isolation of the hemodynamic response (HDR) for each task epoch. All extracted functional networks displayed statistically significant sensitivity to delay length. Novel information extracted from these networks that was not apparent in the univariate analysis of these data included involvement of the hippocampus in encoding/probe, and decreases in BOLD signal in the superior temporal gyrus (STG), along with default-mode regions, during encoding/delay. The bilateral hippocampal activity during encoding/delay fits with theoretical models of WM in which memoranda held across the short term are activated long-term memory representations. The BOLD signal decreases in the STG were unexpected, and may reflect repetition suppression effects invoked by internal repetition of letter stimuli. Thus, analysis methods focusing on how network dynamics relate to experimental conditions allowed extraction of novel information not apparent in univariate analyses, and are particularly recommended for WM experiments for which task epochs cannot be randomized.

Introduction

Working memory (WM) refers to the ability to actively hold information in mind in the service of guiding behavior (Baddeley and Hitch, 1974). It is not a unitary construct and there are distinct cognitive processes involved in encoding information, maintaining it on-line, and selecting a response. Event-related functional MRI (fMRI) investigations of WM have identified individual brain regions subserving the cognitive processes engaged by each of these task requirements by manipulating and contrasting task conditions to isolate activation for each task epoch. Since cognitive functions depend on coordinated activity in distributed networks, this approach is inherently limited, in that regions that show similar significant differences in the magnitude of activation for a particular contrast need not comprise a functional network. Several cognitive processes are involved in each WM task epoch, and each may rely on distinct networks. The goal of the present study was to employ a combination of experimental design and analysis methodology that allows determination of dynamic changes in network involvement across temporally distinct WM task epochs.

To accomplish this, we reanalyzed the data from a previously published rapid-presentation event-related fMRI study (Manoach et al., 2003). This WM task design had several attributes that facilitated linking of functional networks to temporally-separated WM epochs. During all WM experiments, encoding must precede maintenance over a delay, and the response must follow. Since the order of events cannot be randomized, the assignment of neural activity to specific task epochs is challenging. In the current task design, the length of the delay period was manipulated to facilitate identification of activation affiliated with each task epoch, based on the shape of the hemodynamic response (HDR). For example, networks engaged by processes necessary for maintenance over a delay would be expected to show a more prolonged HDR with longer delays. Similarly, the HDR of networks involved in only the probe epoch should show a staggered onset time, depending on the length of the preceding delay period.

* Corresponding author at: Room A3-A116, BC Mental Health & Addictions Research Institute, Translational Research Building, 3rd Floor, 938 W. 28th Avenue, Vancouver, British Columbia, Canada V5Z 4H4. Fax: +1 604 875 3871.
E-mail address: todd.woodward@ubc.ca (T.S. Woodward).

1053-8119/$ – see front matter © 2012 Elsevier Inc. All rights reserved.
http://dx.doi.org/10.1016/j.neuroimage.2012.09.070

The multivariate analysis technique used to identify brain regions showing temporally correlated activation (i.e., functional networks) corresponding to each task epoch was constrained principal component analysis for fMRI (fMRI-CPCA). fMRI-CPCA combines multivariate regression and principal component analysis to derive networks from the portion of variability in the blood-oxygen level dependent (BOLD) signal that can be explained by the timing of task events. CPCA differs from other approaches to examining correlations in activation among regions in that it identifies functional networks that are based on *task-related* covariance/correlation in BOLD signal. It also estimates the HDR for each network by using a finite impulse response (FIR) model (Henson et al., 2001; Manoach et al., 2003; Metzak et al., 2011; Metzak et al., 2012; Rapin et al., 2012), which makes no a priori assumptions concerning the shape of the HDR, and provides an estimate of the amplitude of the average BOLD response at each time point, and for each subject separately (Burock and Dale, 2000; Dale and Buckner, 1997; Glover, 1999; Henson et al., 2001; Serences, 2004). Although innovative experimental design is required for accurately separating and assigning signal to task epochs, optimal analysis methods complement an informative design by identifying patterns in the signal that summarize the data and suggest network architecture that subserves cognitive function.

Based on prior findings (Manoach et al., 2003; Metzak et al., 2011; Metzak et al., 2012; Postle, 2006), we expected the encoding and delay epochs to be associated with networks composed of primary and association visual cortices, and the probe epoch to be associated with activation in networks involved in executive control over motor responses, including the anterior cingulate cortex, primary and premotor cortices, inferior prefrontal cortex, and basal ganglia. We did not expect unique networks to be involved in the delay epoch, but rather an overlap of delay networks with those associated with encode and probe epochs, since maintenance of information is required across all task epochs.

Methods

Details regarding the task design, sample characteristics and data acquisition have been published previously (Manoach et al., 2003), and a summary is presented here (see Fig. 1 for a depiction of task timing). Of the original 12 participants, the data for two were corrupted and could not be retrieved. The ten remaining participants were right-handed, healthy, native English speakers (6 female, mean age 29.67 years, age range 22–46, SD = 6.88). Each WM trial began with a central fixation cross for 500 ms followed by the presentation of a set of five digits (targets) to be learned (3500 ms; encode epoch). This was followed by the delay epoch during which time the screen was blank. During the probe epoch, subjects were presented with a single digit (probe) for 2000 ms. In half the trials the probe was a target (a member of the memorized set) and in the other half the probe was a foil (not a member of the memorized set). Subjects responded by pressing a button box with their right thumb for targets and their left thumb for foils. The three trial types differed only in the length of the delay period that lasted either 0 s (D0), 2 s (D2), or 4 s (D4). The three trial types randomly alternated with a fixation baseline condition within each run. During the baseline condition, subjects fixated on an asterisk that appeared in the center of the screen. The duration of fixation randomly varied in increments of 2 s up to a maximum of 12 s. Subjects performed six runs of 4 min 48 s each. Each run contained nine trials of each WM condition and 72 s of fixation. The total experiment time was approximately 35 min.

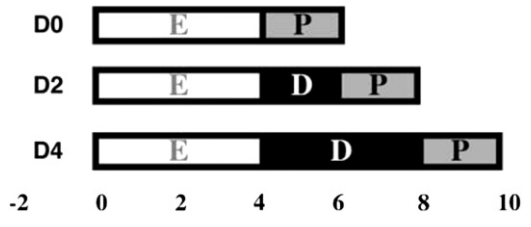

Fig. 1. The timing (in seconds) of the epochs in the three WM trial types (D0, D2, D4). E = encoding (4 s). P = probe (2 s). D = delay (0, 2 or 4 s).

Constrained principal component analysis for fMRI

The details of fMRI-CPCA analyses using an FIR model are presented elsewhere (Metzak et al., 2011; Metzak et al., 2012; Woodward et al., 2006). For the comprehensive CPCA theory and proofs please see previously published work (Hunter and Takane, 2002; Takane and Hunter, 2001; Takane and Shibayama, 1991). The fMRI-CPCA application is available on-line, free of charge (www.nitrc.org/projects/fmricpca). Briefly, after variance in the BOLD signal attributable to the task has been separated from that not attributable to the task, the dominant patterns of inter-correlation between voxels over time are used to derive functional networks. The use of an FIR model allows a HDR shape to be derived for each functional network identified. To confirm the reliability of the components, for each functional network (component) extracted, we conducted repeated-measures analyses of variance (ANOVAs), whereby significant interactions between peristimulus time and the delay period duration would suggest that the shape of the HDR was affected by variation in delay length. Visual inspection of the HDRs and post-hoc contrasts of time points across conditions enabled assignment of each functional network to one or more task epochs.

We now briefly present matrix equations for the current application of CPCA which required preparation of two matrices. The first matrix, *Z*, contained the BOLD time series of each voxel, with one column per voxel and one row per scan. Each column contained normalized and smoothed activations over all scans, for each subject separately. The second matrix, *G*, contained FIR models of the expected BOLD response to the timing of stimulus presentations.

Preparation of G

The *G* (design) matrix consisted of a FIR basis set, which can be used to estimate the increase in BOLD signal at specific peristimulus scans relative to all other scans. The value 1 is placed in rows of *G* for which BOLD signal amplitude is to be estimated, and the value 0 in all other rows ("mini boxcar" functions). The time points for which a basis function was specified in the current study were the 1st to 10th scans following stimulus presentation. Since the repetition time (TR) for these data was 2 s, this resulted in estimating BOLD signal over a 20 s window, with the start of the first time point (time = 0) corresponding to encoding stimulus onset. In this analysis we created a G matrix that would allow us to estimate subject-and-condition specific effects by inserting a separate FIR basis set for each delay duration condition and for each individual subject. The columns in this subject-and-condition based *G* matrix code 10 peristimulus time points, 3 delay conditions, and 10 subjects, resulting in 300 columns ($10 \times 3 \times 10 = 300$).

Matrix equations

The matrix of BOLD time series and design matrices are taken as input, with BOLD in *Z* being predicted from the FIR model in *G*. In order to achieve this, multivariate least-squares linear regression was carried out, whereby the BOLD time series (*Z*) was regressed onto the design matrix (*G*):

$$Z = GC + E \tag{1}$$

where $C = \left(G'G\right)^{-1}G'Z$, or least squares multivariate multiple regression. This analysis yielded condition-specific regression weights in the *C* matrix (i.e., regression weights specific to the experimental conditions as defined by the design matrix). The condition-specific regression

weights are often referred to (in conventional fMRI analyses) as beta images. *GC* contained variability in *Z* that was predictable from the design matrix *G*, that is to say, variability in *Z* that was predictable from the timing of stimulus presentations. For the analysis presented here, the *G* matrix was standardized for each subject separately.

The next step employed singular value decomposition to extract components representing networks of functionally interconnected voxel activations from *GC* that were related to the experimental stimulus presentations. This involved singular value decomposition of the activation variability that was predictable from the design matrix (*GC*):

$$UDV' = GC \quad (2)$$

where U = matrix of left singular vectors; D = diagonal matrix of singular values; and V = matrix of right singular vectors. Each column of *VD* can be overlaid on a structural brain image to allow visualization of the neural regions involved in each functional network. In the current application of CPCA, following dimension reduction, we orthogonally rotated (Metzak et al., 2011) and rescaled the *VD* matrix prior to display, so that a rotated *loading matrix* is displayed. The values of the loading matrix contain the correlations between the components in *U* and the variables in *GC*. An orthonormal rotation transformation matrix is then used to transform the rescaled left singular vectors *U* into rotated component scores (with rows corresponding to scans).

Predictor weights

To interpret the components with respect to the conditions represented in *G*, we produced *predictor weights* (Hunter and Takane, 2002) in matrix *P*. These are the weights that would be applied to each column of the matrix of predictor variables (*G*) to create *U* ($U = GP$) and can be orthogonally rotated by applying the same transformation matrix (Metzak et al., 2011) as was applied to *VD* and *U*. The values in *P* indicate the importance of each column in the *G* matrix to the network(s) represented by the component(s), so are essential for relating the resultant components to the experimental conditions of interest represented in *G*. This approach estimates an HDR shape for each individual separately, so it fully accommodates this heterogeneity.

Statistical tests of component reliability and the delay period manipulation

As is explained above, predictor weights are produced for each combination of peristimulus time point, delay condition, and subject. These weights can be used to statistically test the effect of peristimulus time, to determine whether or not these values are reflecting a HDR shape (and not, for example, simply varying randomly around zero). The impact of the experimental conditions on the estimated HDR shapes can also be tested statistically. In the current study, the experimental condition is the manipulation of the duration of the delay period. This would be reflected by a significant interaction between peristimulus time and the delay period duration for the measure of estimated HDR (i.e., the predictor weights). Omitting the first point of peristimulus time (which was adjusted to zero for predictor weights in all conditions for the purposes of display and data analysis), this analysis would be carried out as a 9×3 repeated-measures ANOVAs for each component, with the factors of Time Point (time points 2–10 after the initiation of a task trial) and Delay (D0, D2, D4) as within-subject factors. Selecting "repeated" contrasts for the within-subjects factor of Delay and Time Point allows significance tests to be restricted to adjacent time points and/or adjacent delay manipulation conditions. This allows the complex 9×3 interactions between Time Point and Delay to be broken down into 16 different 2×2 interactions involving adjacent levels of the Time Point and Delay factors. Inspection of the relative size of the *p* values for these 16 different 2×2 interactions can pinpoint the time points that provide main sources of the 9×3 interactions (e.g., from the 5 to 7 second time points, a significant increase in the D0 vs. D2 pairwise comparison can be observed). Visual inspection of the HDR shapes while considering the experimental design (delay period manipulation) facilitates assignment of each network to one or more task epochs. Tests of sphericity were carried out for all ANOVAs. Greenhouse–Geisser adjusted degrees of freedom for violations of sphericity were inspected but did not affect the results; therefore, the original degrees of freedom are reported. Since our significance testing is carried out at the level of subject-specific HDR estimates, the requirement to use bootstrapping to produce *Z*-map images is negated. Therefore, point estimates (i.e., the orthogonally rotated *VD* matrix) are overlaid on structural brain images for depiction of the spatial arrangement of the functional networks.

Results

Behavior

Repeated measures ANOVAs revealed no significant effect of the delay length on accuracy, $F(2,18) = 0.44$, $p = 0.65$ (percent correct: D0 = 96.8; D2 = 97.4; D4 = 96.7) or RT, $F(2,18) = 1.85$, $p = 0.19$ (D0 = 904 ms; D2 = 910 ms; D4 = 886 ms).

Activations

Inspection of the scree plot indicated that four components should be extracted for further significance testing. The sum of the squared loadings divided by the number of scans (analogous to the percentage of *GC* variance accounted for by each component) for the rotated solution was 24.8, 16.0, 11.9 and 6.0 for Components 1, 2, 3 and 4, respectively. The neural regions comprising the functional networks represented by each component, mapped onto an MNI structural image, are displayed in Figs. 2A–D (top panels), with corresponding anatomical descriptions in Tables 1–4.

The mean predictor weights plotted as a function of peristimulus time, representing the estimated HDR of each functional network, are listed in Figs. 2A–D (bottom panels). The repeated-measures ANOVAs of the predictor weights for each component resulted in highly significant Time Point × Delay (9×3) interactions, indicating that the magnitude and/or shape of the HDR was dependent on the delay period manipulation. The dominant 2×2 interactions are listed below to pinpoint the time points that are the main sources of the 9×3 interactions.

Anatomical descriptions and relation to experimental conditions

Component 1. Component 1 (9×3 interaction, $F(16, 144) = 7.25$, $p < 0.001$, $\eta^2 = 0.45$) involved primarily visual cortex regions, including primary visual cortex (peaks in Brodmann areas (BAs) 17, 18), as well as left precentral gyrus and supplementary motor area, right angular gyrus, and bilateral hippocampi. Visual inspection of the HDR (Fig. 2A) suggests that activity in this network corresponded with trial onset, and that the significant interaction reflects a bimodal peak for the D4 condition, contrasted with a unimodal peak for the D0 condition, with D2 falling in between. When the delay period is absent (D0), the estimated HDR is sustained relative to the other conditions, peaking at approximately 7–9 s, and reducing to baseline by 15 s. As the delay period increased in D2 and D4, the estimated HDR became more bimodal, suggesting that this functional network was responding to the visual demands of the encode and probe epochs, but not the delay epoch, during which participants viewed a blank screen. This functional network was labeled *Encoding/Probe*.

Component 2. Component 2 (9×3 interaction, $F(16, 144) = 47.54$, $p < 0.001$, $\eta^2 = 0.84$) was characterized primarily by activation in bilateral insula, bilateral thalamus, bilateral cerebellum, bilateral sensorimotor regions, and bilateral dorsal anterior cingulate cortex. Also present were motor-related regions surrounding the central sulcus extending into the pre- and postcentral gyri and sulci, and also in

Table 1
Cluster volumes for most extreme 10% of Component 1 (*Encoding/Probe*) loadings, with anatomical descriptions, MNI coordinates, and Brodmann area for the peaks within each cluster. Only clusters >270 mm^3 are presented here.

Cortical regions	Cluster volume (mm^3)	Cluster volume (voxels)	Brodmann area for peak locations	MNI coordinate (X Y Z) for peak locations			Loading value
Positive loadings							
Cluster 1: bilateral	135,864	5032					
Occipital pole			17	15	−93	−3	0.41
Occipital pole			18	−9	−96	−6	0.41
Inferior lateral occipital cortex			19	−39	−78	−18	0.40
Inferior lateral occipital cortex			19	42	−87	−6	0.35
Superior lateral occipital cortex			19	−27	−81	24	0.31
Superior lateral occipital cortex			19	33	−78	24	0.29
Cerebellum — Crus I			N/A	−39	−60	−30	0.26
Lingual gyrus			18	−18	−78	0	0.26
Superior parietal lobule			7	−27	−54	45	0.26
Cerebellum — Crus II			N/A	3	−84	−30	0.25
Cluster 2: left hemisphere	6075	225					
Precentral gyrus			6	−51	−3	42	0.29
Cluster 3: left hemisphere	4185	155					
Supplementary motor area			6	−3	0	63	0.28
Cluster 4: right hemisphere	1782	66					
Angular gyrus			7	33	−63	51	0.25
Cluster 5: right hemisphere	1458	54					
Hippocampus			27	27	−30	−6	0.26
Cluster 5: left hemisphere	1350	50					
Hippocampus			27	−24	−30	−6	0.25

the cerebellum. Visual inspection of the HDR in Fig. 2B suggests that the significant interaction was due to the estimated HDR initiating activity in a staggered fashion with peaks at approximately 9, 11 and 13 s corresponding to the onset of the probe epoch, indicating a role for this network in generating a response, but not in encoding or delay. This functional network was labeled *Probe*.

Component 3. Component 3 (9×3 interaction, $F(16, 144) = 5.19$, $p<0.001$, $\eta^2 = 0.37$) included bilateral activation in the occipital pole, but was dominated by BOLD signal decreases in the superior temporal gyrus (STG), inferior parietal cortex, posterior cingulate cortex/precuneus, and several parts of the prefrontal cortex. Visual inspection of the HDR in Fig. 2C suggests that network intensity (primarily BOLD signal decreases) began at trial onset (suggesting that it was involved in encoding). The earlier peak for D0, which was sharper than that in *Encoding/Probe* (Fig. 2A), and the absence of any increase in activity for D4 later than 11 s, suggests that this component was *not* involved in the probe epoch, but was involved in encoding, and to a lesser extent, delay. This functional network was labeled *Encoding/Delay*.

Component 4. Component 4 (9×3 interaction, $F(16, 144) = 9.19$, $p<0.001$, $\eta^2 = 0.68$) was primarily restricted to the medial occipital cortices. Visual inspection of the HDR in Fig. 2D suggests that this interaction was due to an earlier decline in the HDR for D0 relative to D2 (13 and 15 second downward peaks), an earlier peak for D2 than D4 (15 and 17 second peaks), as well as staggered onsets corresponding to the delay period manipulations. However, this component does not appear to be involved in the probe epoch, because the peaks are later than the peristimulus time observed for clearly probe-epoch activity (i.e., those for Component 2). Close inspection of the previously published univariate results (Manoach et al., 2003, Figure 3, #14, #15, #16, #17) suggests that for the primary visual cortex, fusiform and lingual gyrus areas, an undershoot of the HDR function is present at the completion of the WM trial, resulting in a functional network in the current analysis. Component 4 intensified at the completion of the trial, and therefore the onsets of the HDRs are staggered, because increased delay length translates directly into increased trial length; however, Component 4 is not active during the delay period. This functional network was labeled *Undershoot*.

Dominant 2×2 interactions

Component 1. The dominant 2×2 interactions of adjacent factor levels (that provide the main source of the 9×3 interaction) indicated that (1) the D0 vs. D2 pairwise comparison reversed direction (from D0>D2 to D0<D2) over the 7 to 9 second time points ($p<.01$), reversed back over the 11 to 13 second time points ($p<.005$) and then reduced from a large difference (D2>D0) to no difference (baseline) over the 15 to 17 second time points ($p<.01$).
(2) The D2 vs. D4 pairwise comparison (D2>D4) increased magnitude over the 9 to 11 second time points ($p<.05$), changing from equivalent to large (D4>D2) over the 13 to 15 second time points ($p<.05$), and then reducing from large (D4>D2) back to equivalent (baseline) over the 17 to 19 second time points ($p<05$).

Component 2. The dominant 2×2 interactions of adjacent factor levels (that provide the main source of the 9×3 interaction) indicated that (1) the D0 vs. D2 pairwise comparison reversed direction over the 9 to 11 second time points ($p<.001$), and decreased substantially (D2>D0) over the 13 to 15 ($p<.001$) and 15 to 17 ($p<.001$) second time points, such that both D2 and D0 were equivalent (and at baseline) by 17 seconds. (2) The D2 vs. D4 pairwise comparison reversed direction over the 11 to 13 second time points ($p<.001$), and decreased substantially (D2>D0) over the 15 to 17 second time points ($p<.001$), such that both D4 and D2 were equivalent (and at baseline) by 17 seconds.

Component 3. The dominant 2×2 interactions of adjacent factor levels (that provide the main source of the 9×3 interaction) indicated that (1) the D0 vs. D2 pairwise comparison increased magnitude (D0>D2) over the 5 to 7 second time points ($p<.05$), and reversed

Table 2
Cluster volumes for most extreme 10% of Component 2 (*Probe*) loadings, with anatomical descriptions, MNI coordinates, and Brodmann area for the peaks within each cluster. Only clusters >270 mm^3 are presented here.

Cortical regions	Cluster volume (mm^3)	Cluster volume (voxels)	Brodmann area for peak locations	MNI coordinate (X Y Z) for peak locations			Loading value
Positive loadings							
Cluster 1: bilateral	72,414	2682					
Supplementary motor area			32	−6	6	48	0.33
Anterior cingulate gyrus			32	6	15	45	0.30
Postcentral gyrus			2	–48	−30	45	0.30
Anterior supramarginal gyrus			40	−42	−39	39	0.29
Superior parietal lobule			2	−42	−39	54	0.28
Central opercular cortex			42	−42	−39	54	0.27
Middle frontal gyrus			6	−27	−6	54	0.27
Cluster 2: right hemisphere	28,836	1068					
Precentral gyrus			6	42	−15	54	0.28
Postcentral gyrus			3	45	−24	42	0.27
Middle frontal gyrus			6	30	−3	57	0.26
Parietal operculum cortex			42	57	−21	15	0.22
Cluster 3: left hemisphere	15,498	574					
Insula			N/A	−30	18	−3	0.28
Precentral gyrus			6	−57	9	21	0.25
Central opercular cortex			N/A	−48	0	3	0.24
Cluster 4: right hemisphere	9575	355					
Orbitofrontal cortex			47	33	24	−6	0.27
Frontal operculum cortex			47	45	18	0	0.23
Inferior frontal gyrus (pars opercularis)			45	54	15	0	0.22
Precentral gyrus			6	57	9	15	0.20
Cluster 5: bilateral	7884	292					
Cerebellum — Lobule VI			N/A	−24	−57	−33	0.24
Cerebellum — Vermis VI			N/A	3	−72	−24	0.21
Cerebellum — Vermis VI			N/A	−3	−66	−18	0.21
Cluster 6: right hemisphere	6399	237					
Cerebellum — Lobule VI			N/A	30	−57	−33	0.26
Cluster 7: right hemisphere	4644	172					
Thalamus			N/A	12	−18	3	0.25
Cluster 8: left hemisphere	4185	155					
Thalamus			N/A	−12	−18	0	0.25
Cluster 9: left hemisphere	594	22					
Middle frontal gyrus			45	−42	33	18	0.21
Cluster 10: left hemisphere	513	19					
Inferior lateral occipital cortex			37	−51	−66	−6	0.21

direction over the 7 to 9 second time points ($p<.01$). (2) The D2 vs. D4 pairwise comparison increased magnitude (D2>D4) over the 7 to 9 second time points ($p<.01$), reducing back to no difference over the 9 to 11 second time points ($p<.05$), followed by a reversal (D4>D2) over the 11 to 13 second time points ($p<.10$) with this difference again returning to equivalence (and at baseline) over the 15 to 17 second time points ($p<.05$).

Component 4. The dominant 2×2 interactions of adjacent factor levels (that provide main source of the 9×3 interaction) indicated that (1) the D0 vs. D2 pairwise comparison increased substantially (D0<D2) over the 9 to 11 second time points ($p<.01$), decreased substantially over the 11 to 13 second time points ($p<.05$), reversed over the 13 to 15 second time points ($p<.05$), and reduced from 17 to 19 second time points such that both D2 and D0 were equivalent (and at baseline) by 19 s. (2) The D2 vs. D4 pairwise comparison increased substantially (D2<D4) over the 11 to 13 second time points ($p<.05$), decreased substantially over the 13 to 15 second time points ($p<.05$), and reversed over the 15 to 17 second time points ($p<.01$).

Discussion

In the current study, functional networks involved in the temporally-separated epochs of a WM task were identified. This approach complemented and extended the previous univariate analysis by providing novel insights into the dynamics of network activity across the temporally separated epochs of WM performance. Functional networks were extracted that engaged during encoding, delay, and response epochs, and all extracted networks displayed statistically significant sensitivity to delay length. Novel information extracted from these networks (that was not apparent in the univariate analysis of these data) included involvement of the hippocampus in encoding/probe, and BOLD signal decreases in default-mode regions and the superior temporal gyrus (STG) during encoding/delay. Thus, framing results in terms of how network dynamics relate to experimental conditions allowed extraction of novel information not apparent in univariate analyses, including better defined anatomical depictions, effective temporal separation of WM epochs, and simultaneous relation of anatomical depictions and WM epochs.

Table 3
Cluster volumes for most extreme 10% of Component 3 (*Encoding/Delay*) loadings, with anatomical descriptions, MNI coordinates, and Brodmann area for the peaks within each cluster. Only clusters >270 mm^3 are presented here. Positive and negative loadings are presented in the top and bottom sections of the table, respectively.

Cortical regions	Cluster volume (mm^3)	Cluster volume (voxels)	Brodmann area for peak locations	MNI coordinate (X Y Z) for peak locations			Loading value
Positive loadings							
Cluster 1: left hemisphere	5130	190					
Occipital pole			18	−12	−96	−6	0.26
Cerebellum — Crus I			N/A	−18	−87	−21	0.15
Cluster 2: right hemisphere	5103	189					
Occipital pole			18	18	−96	−3	0.24
Cluster 3: left hemisphere							
Cerebellum — Crus I	513	19	N/A	−30	−84	−24	0.19
Negative loadings							
Cluster 1: left hemisphere	62,181	2303					
Parietal opercular cortex			42	−60	−36	21	−0.21
Heschl's gyrus			22	−54	−12	0	−0.20
Postcentral gyrus			2	−63	−24	30	−0.19
Insula			N/A	−39	−21	0	−0.19
Angular gyrus			39	−54	−57	33	−0.19
Planum polare			22	−42	−18	−3	−0.19
Inferior lateral occipital cortex			37	−57	−66	12	−0.19
Planum temporale			22	−60	−30	12	−0.19
Superior lateral occipital cortex			39	−57	−63	21	−0.19
Supramarginal gyrus			40	−60	−42	33	−0.19
Inferior lateral occipital cortex			37	−45	−63	15	−0.19
Superior parietal lobule			5	−21	−54	66	−0.18
Superior temporal gyrus			21	−51	−3	−12	−0.17
Precentral gyrus			6	−24	−15	66	−0.17
Central opercular cortex			N/A	−42	−15	15	−0.16
Middle temporal gyrus			21	−54	−3	−27	−0.15
Cluster 2: right hemisphere	57,240	2120					
Planum temporale			22	54	−15	3	−0.22
Supramarginal gyrus			40	66	−24	24	−0.20
Parietal operculum cortex			42	60	−27	18	−0.20
Superior temporal gyrus			22	57	−9	−6	−0.20
Planum polare			21	51	0	−9	−0.19
Insula			N/A	39	24	9	−0.19
Frontal pole			47	45	39	−3	−0.18
Inferior frontal gyrus (pars triangularis)			45	51	24	9	−0.18
Superior lateral occipital cortex			39	57	−63	27	−0.18
Inferior frontal gyrus (pars opercularis)			45	54	18	6	−0.18
Angular gyrus			40	63	−51	30	−0.17
Putamen			N/A	30	−15	6	−0.16
Superior parietal lobule			3	27	−42	54	−0.16
Middle frontal gyrus			6	48	6	6	−0.16
Middle temporal gyrus			21	54	−6	−21	−0.15
Cluster 3: bilateral	5292	196					
Precuneus			7	−3	−57	48	−0.17
Posterior cingulate cortex			23	−3	−33	42	−0.16
Cluster 4: bilateral	3672	136					
Anterior cingulate gyrus			32	−3	36	33	−0.17
Superior frontal gyrus			8	3	30	48	−0.17
Cluster 5: right hemisphere	2484	92					
Frontal pole			9	30	42	36	−0.16
Middle frontal gyrus			9	42	18	45	−0.16
Superior frontal gyrus			8	24	24	48	−0.15
Cluster 6: bilateral	1593	59					
Anterior cingulate cortex			24	0	21	15	−0.16
Cluster 7: right hemisphere	1593	59					
Superior parietal lobule			7	24	−45	69	−0.17
Superior lateral occipital cortex			5	15	−57	66	−0.16
Precuneus			7	9	−60	57	−0.16
Postcentral gyrus			3	33	−36	66	−0.15
Cluster 8: left hemisphere	999	37					
Middle frontal gyrus			9	−42	12	45	−0.16
Superior frontal gyrus			9	−21	27	42	−0.15
Cluster 9: right hemisphere	837	31					
Middle temporal gyrus			37	63	60	−3	−0.17

Table 3 (*continued*)

Cortical regions	Cluster volume (mm^3)	Cluster volume (voxels)	Brodmann area for peak locations	MNI coordinate (X Y Z) for peak locations			Loading value
Negative loadings							
Cluster 10: left hemisphere	513	19					
Superior frontal gyrus			8	−21	21	48	−0.15
Cluster 11: bilateral	378	14					
Cuneus			18	−3	−81	33	−0.16
Cluster 12: right hemisphere	378	14					
Superior lateral occipital cortex			7	9	−75	54	−0.16
Cluster 13: left hemisphere	351	13					
Middle temporal gyrus			20	−54	−48	−9	−0.17
Cluster 14: right hemisphere	351	13					
Frontal pole			11	24	48	−6	−0.16
Cluster 15: bilateral	297	11					
Posterior cingulate cortex			23	12	−21	42	−0.15

Table 4
Cluster volumes for most extreme 10% of Component 4 (*Undershoot*) loadings, with anatomical descriptions, MNI coordinates, and Brodmann area for the peaks within each cluster. Only clusters >270 mm^3 are presented here.

Cortical regions	Cluster volume (voxels)	Cluster volume (voxels)	Brodmann area for peak locations	MNI coordinate (X Y Z) for peak locations			Loading value
Positive loadings							
Cluster 1: bilateral	133,164	4932					
Lingual gyrus			18	−12	−78	−9	0.29
Occipital fusiform gyrus			18	21	−78	−12	0.28
Intracalcarine cortex			17	12	−72	9	0.24
Cuneus			18	−6	−87	18	0.23
Occipital pole			17	21	−99	18	0.22
Supracalcarine cortex			18	6	−75	18	0.22
Temporal fusiform cortex			37	−27	−39	−18	0.15
Superior lateral occipital cortex			39	−48	−75	27	0.11
Cluster 2: left hemisphere	5400	200					
Precentral gyrus			6	−51	−6	42	0.17
Postcentral gyrus			4	−42	−21	45	0.13
Cluster 3: bilateral	4023	149					
Brain stem			N/A	6	−27	−12	0.14
Cluster 4: right hemisphere	2133	79					
Precentral gyrus			6	54	−3	51	0.14
Cluster 5: *bilateral*	1512	56					
Supplementary motor area			6	−6	0	60	0.14
Anterior cingulate gyrus			6	−9	12	51	0.14
Cluster 6: left hemisphere	891	33					
Planum temporale			41	−48	−39	18	0.13
Cluster 7: right hemisphere	486	18					
Middle temporal gyrus			20	54	−12	−21	0.13
Negative loadings							
Cluster 1: bilateral	1458	54					
Posterior cingulate cortex			29	−60	−36	21	−0.14
Cluster 2: right hemisphere	621	23					
Caudate			N/A	18	−3	21	−0.13
Cluster 3: left hemisphere	405	15					
Hippocampus			N/A	−18	−45	9	−0.14

According to the univariate results, encoding was expected to be associated with visual association and primary visual cortices (Manoach et al., 2003, Figure 3, #13, #16, #17), and this emerged in the *Encoding*/*Probe* network with the HDR pattern expected for visual activity associated with encoding and probe (viz., simultaneous initiation of activation, and gradually bimodal peaks emerging with delay, with full bimodality in D4; Fig. 2A). Although the univariate results suggested that the response of visual regions to the probe was not significant, the CPCA results demonstrated that when the signal common to visual regions is analyzed, they respond to the probe as well as to the to-be-encoded stimuli (albeit to a lesser extent). This replicates the results of a previous fMRI-CPCA analysis on WM data (Metzak et al., 2011) and the involvement of frontal and parietal regions is consistent with other accounts (Duncan and Owen, 2000). Interestingly, this functional network also involved bilateral hippocampus, not apparent in the univariate analysis. This fits with other neuroimaging results, as well as with theoretical models of WM in which memoranda held across the short term are activated long-term memory representations (Cowan, 1995; Lewis-Peacock and Postle, 2008; Oberauer, 2002; Oztekin et al., 2010; Ranganath et al., 2004). Thus, encoding digit stimuli into WM and recognition/retrieval-related processes appears to recruit a network involving the hippocampus, early visual cortex (including areas sensitive to letter stimuli; Vinckier et al., 2007), and fronto-parietal areas, identified from a WM meta-analysis as part of a consistently activated set of regions forming a "core" WM network (Rottschy et al., 2012).

According to the univariate results, we expected that the probe epoch would be associated with activation in the dorsolateral prefrontal cortex (DLPFC), dorsal anterior cingulate cortex, inferior frontal regions, insula and thalamus (Figure 3 #5, #11, #10, #7; Figure 4 #18, #19 in Manoach et al., 2003, for univariate results). Suggestions for why DLPFC activation was absent for the delay period in this task were presented in the discussion section of the original univariate analysis (Manoach et al., 2003) and are not repeated here. The functional network associated with *Probe* showed activation in several of these regions, along with the time course that would be expected for a network involved in the probe epoch. Possibly because of the focus on patterns of intercorrelation between regions, the clusters seen in the CPCA results for these regions (Fig. 2B) appear better defined than those from the univariate analysis (Manoach et al., 2003, Figure 3), and the estimated HDR is sharper, very clearly demonstrating the temporally staggered pattern expected as a result of increasing delay epoch length. This suggests that this network subserves cognitive processes required during the probe epoch, such as scanning the contents of WM, comparing the probe to items in the memorized set, and selecting and generating the appropriate response (Bledowski et al., 2012; Kahana and Sekuler, 2002; Sternberg, 1966). DLPFC involvement in the probe was expected due to the univariate results, but these involved small clusters (Figure 3, #1 and #5). Correspondingly, although not displayed in Table 2 and Fig. 2B, the DLPFC was involved in the Probe component, but these clusters were not greater than 270 mm^3 displayed in Fig. 2B (left side cluster peak MNI XYZ: −35, 55, 16; BA 46; loading = 0.19; right cluster peak MNI XYZ: 35, 45, 22; BA 46; loading = 0.17). The left inferior frontal cluster is consistent with previous findings for this task epoch (Buchsbaum et al., 2005a; Derrfuss et al., 2004; Oztekin et al., 2009). The IFG cluster also includes Broca's area, a well-known locus for speech production and therefore some of the areas comprising this network fit with an emergent property model of WM (Postle, 2006) in which regions representing information under non-sensory conditions also could maintain the same information across delay periods for subsequent retrieval. In addition to Broca's area, anterior insula, supplementary motor area, basal ganglia, and postcentral and superior temporal gyri have all been implicated in the motor control of speech (e.g., Price et al., 2011; Riecker et al., 2005). Indeed, involvement of language-related areas in WM was recently demonstrated directly with transcranial magnetic stimulation (Acheson et al., 2011) and in a patient lesion study (Koenigs et al., 2011). We therefore suggest that this network might invoke speech production-related processes during the probe phase of the task.

Because this *Probe* network is separate from *Encoding*/*Probe*, it might be that several parallel processes are engaged for recognition of the probe, such as context reinstatement (indexed by *Encoding*/*Probe*) and the aforementioned speech production processes (indexed by *Probe*) although the precise nature of such processes and any possible interaction between them, is not clear from the current study. What is interesting, however, is that many of the regions that were involved in probe only, or encoding and probe (Figs. 2A and B) in the current multivariate analysis, were instead attributed to combinations of encoding/probe and the delay epoch in the univariate analysis. Examples of such areas are visual association areas, primary sensory cortex, and left primary motor and premotor and supplementary motor regions (Manoach et al., 2003, Figure 3, #9, #8, #2, #12). Univariate estimates of HDR shapes are based on beta weights, which reflect combinations of all underlying functional networks, whereas component loadings and predictor weights allow these networks to be studied separately. As such, in the univariate results, this averaging apparently caused activity to be attributed to the delay epoch.

A small cluster of visual cortex that exhibited HDR shapes sensitive to increasing delay length, thus suggesting a role in the delay period, was detectable in the original univariate analysis (Manoach et al., 2003, Figure 3, #16, #17). However, what was not recognized was that these regions form a functional network with BOLD signal decreases of several regions including default mode network regions and the STG (Fig. 2C). The negative loadings of this component translate in a direct sense to a decrease in BOLD signal (reflected by increasing predictor weights) in response to task demands (relative to task-off periods), and a negative loading is not interpreted differently from a positive loading with respect to how salient this network is at a given point in time. The increase in early visual cortex activity found in the univariate analysis can be attributed to the visual presentation of the digit stimuli during the encoding phase, but the widespread decrease in BOLD signal in frontal, parietal and perisylvian regions that was not detected in the univariate analysis points to a more complex mechanism underlying the encoding and retention of the stimuli than what is suggested by increased activations only.

BOLD signal decreases in the STG during a visual task have been reported as reciprocal activity between primary sensory regions (Hairston et al., 2008; Johnson and Zatorre, 2006; Laurienti et al., 2002; Shulman et al., 1997; Zatorre, 2007), but such an account would predict that BOLD signal decreases in the STG should be sorted into the *Encode*/*Probe* functional network, not the *Encode*/*Delay* network. Perhaps a more plausible explanation lies in the fact that parts of the STG reduce activity during inner speech (Buchsbaum et al., 2005b; Frith et al., 1991), and BOLD signal decreases in the more anterior STG cluster have been reported when repetition of letter stimuli in a WM task produced repetition suppression effects in this area (Buchsbaum and D'Esposito, 2009). One possibility therefore is that this same repetition suppression effect was produced by the current task as the memorized digits cycled through an internal subvocal rehearsal loop. It is also possible that the memory signal might be indexed by activity decreases rather than increases. Indeed, recent work by Lewis-Peacock and Postle (2012) showed that successful recall could occur for stimuli that had displayed delay period activity indistinguishable by a multivariate pattern classifier from a non-memory baseline. We also note here that this specific BOLD signal decrease in the STG replicates previous findings from our group, using similar functional connectivity analysis methodology, but with different Sternberg tasks, different scanners, and different samples (including schizophrenia) (Metzak et al., 2011, Table 1 clusters 1 and 2, BAs 20, 21, 41/42; Metzak et al., 2012, Table 3, clusters 6 and 7 negative loadings, BAs 20, 21).

BOLD signal decreases were also observed in the inferior parietal cortex, posterior cingulate cortex/precuneus, medial prefrontal cortex, and in regions that form part of the task-negative/default-mode

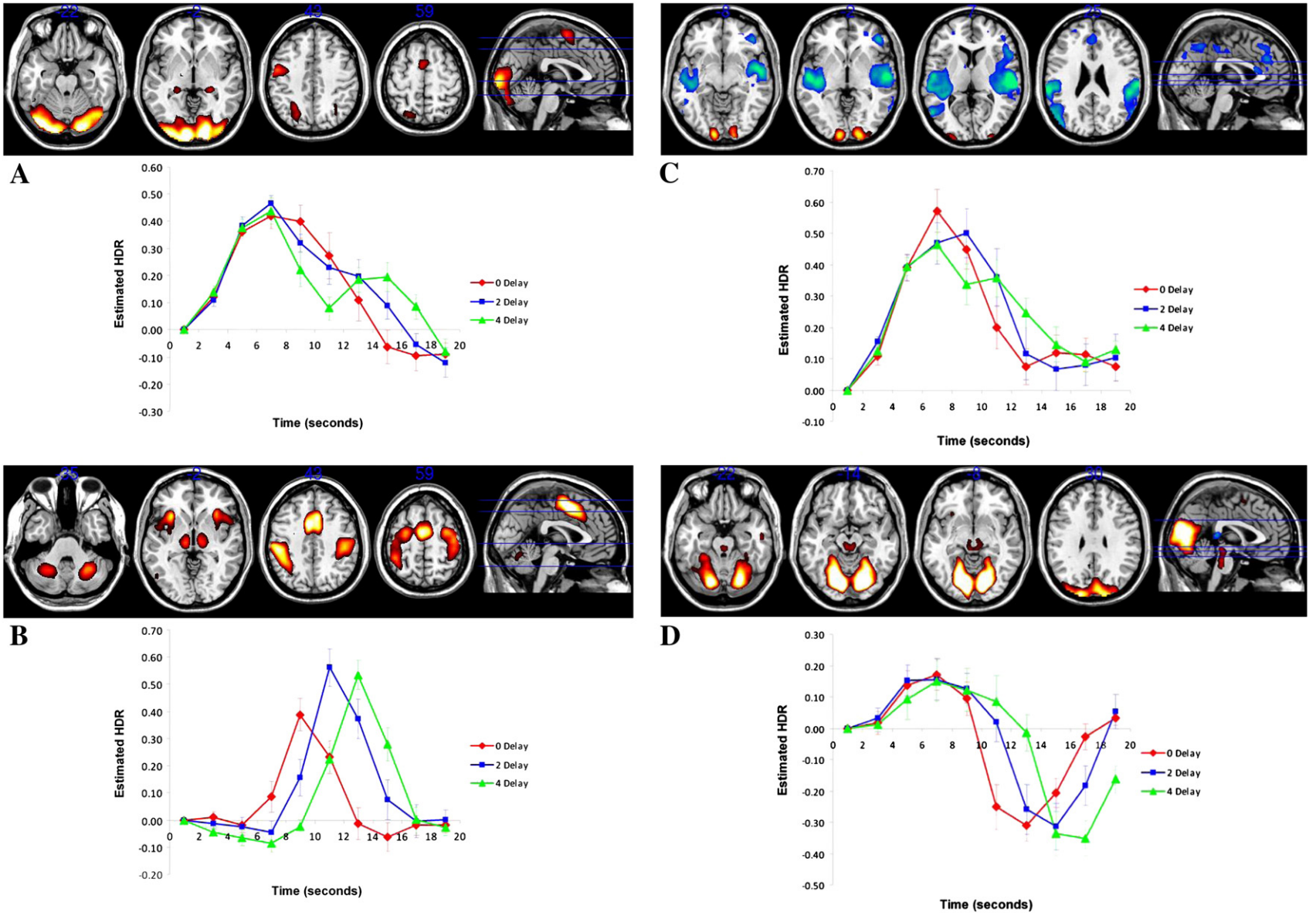

Fig. 2. A–D. Images and plots of predictor weights for Components 1–4. The dominant 10% of component loadings are displayed in the top panel, with positive loadings displayed in red, and negative loadings in blue. Only clusters > 270 mm^3 are displayed. The mean FIR-based predictor weights are plotted as a function of peristimulus time in the bottom panels (error bars are standard errors). The predictor weights are the column of the rotated *P* matrix that was computed alongside each dimension reduced, rotated and rescaled right singular vector (the latter is overlaid on the brain image on the left panel, referred to as component loadings). It is displayed averaged over subjects, where $UT = GPT$, and T is the orthonormal rotation matrix. The predictor weights at the first point of peristimulus time have been adjusted to zero, and all other values scaled accordingly for each subject. A: Component 1 (*Encoding/Probe*); threshold = 0.21, max = 0.41 (no negative loadings passed threshold). Axial slices are located at the following MNI Z-axis coordinates: −22, −2, 43, 59. B: Component 2 (*Probe*); threshold = 0.19, max = 0.33 (no negative loadings passed threshold). Axial slices are located at the following MNI Z-axis coordinates: −35, −2, 43, 59. C: Component 3 (*Encoding/Delay*); threshold = ±0.14, min = −0.26, max = 0.22. Axial slices are located at the following MNI Z-axis coordinates: −8, −2, 7, 25. D: Component 4 (*Undershoot*); threshold = ±0.11, min = −0.14, max = 0.29 (no negative loadings passed the 10% threshold). Axial slices are located at the following MNI Z-axis coordinates: −22, −14, −8, 30.

network (Fox et al., 2005; Raichle et al., 2001). Although it is tempting to explain this as a release of default-mode/task-off activity corresponding to trial onset, this does not accord with the lengthening of the "deactivation" peaks with increase in the length of the delay epoch. More puzzling, however, are the BOLD signal decreases in several regions of the prefrontal cortex, specifically in the superior and middle frontal gyri, a result that is not well supported by previous findings in which activity usually increases in these areas, particularly during encoding. It remains to be tested more directly whether BOLD signal decreases in these regions reflect an actual contribution to encoding and delay-related processes in WM, or whether they are better explained by the ceiling level of task performance, for example. On the whole, however, it does appear that BOLD signal decreases during these task periods are composed of a combination of task-negative and auditory/language-related regions, in addition to the prefrontal regions.

The pattern reflected by *Undershoot* (viz, staggered initiation of activation, very late peaks that do not vary sustained length with delay) appears novel at first glance. However, a close inspection of the univariate results demonstrates evidence for the origin of this component. Specifically, in the original analysis we see that for the primary visual cortex, fusiform and lingual gyrus areas, there is an undershoot of the HDR function that is not present in other areas (Manoach et al., 2003, Figure 3, #14, #15, #16, #17). This was not focused on the univariate results, and correspondingly, *Undershoot* explains a small amount of variance relative to the other components.

A limitation of this analysis methodology is that the fMRI-CPCA approach estimates an HDR shape for each individual separately, so all heterogeneity between subjects is absorbed in the predictor weights. It derives spatial depictions of the networks in terms of what is common to all subjects; therefore, systematic individual differences in spatial representation of the components would be depicted as lower estimated HDRs in the predictor weights only. As is clear from Fig. 2, the standard errors associated with the functional networks (on the predictor weights) are small, indicating that the spatial representations were quite reliable over subjects for this study, but care should be taken, for example, when comparing clinical groups that may possess different network configurations.

This set of results suggests that framing results in terms of how network dynamics relate to experimental conditions allows extraction of novel information not apparent in univariate analyses, including better defined anatomical depictions, effective temporal separation of WM epochs, and simultaneous relation of anatomical depictions. The involvement of the hippocampus in encoding/probe, and BOLD signal decreases in default-mode regions and the STG during encoding/delay were effects not previously detectable using univariate analysis methods. This emphasizes the power of multivariate methodology when attempting to determine the sensitivity of functional networks to experimental conditions and task epochs.

Acknowledgments

TSW is supported by career investigator awards from the Canadian Institutes of Health Research (CIHR) and the Michael Smith Foundation for Health Research (MSFHR). DSM was supported by the National Institute for Mental Health R01 MH67720 and the National Alliance for Research on Schizophrenia and Depression. The authors thank John Paiement for assistance with computer programming, and Jesse Friedman, Liang Wang and Jennifer Riley for assistance in data and manuscript preparation.

References

Acheson, D.J., Hamidi, M., Binder, J.R., Postle, B.R., 2011. A common neural substrate for language production and verbal working memory. J. Cogn. Neurosci. 23, 1358–1367.

Baddeley, A.D., Hitch, G.J., 1974. Working memory. In: Bower, G.A. (Ed.), The Psychology of Learning and Motivation: Advances in Research and Theory. Academic Press, New York, pp. 47–89.

Bledowski, C., Kaiser, J., Wibral, M., Yildiz-Erzberger, K., Rahm, B., 2012. Separable neural bases for subprocesses of recognition in working memory. Cereb. Cortex 22, 1950–1958.

Buchsbaum, B.R., D'Esposito, M., 2009. Repetition suppression and reactivation in auditory-verbal short-term recognition memory. Cereb. Cortex 19, 1474–1485.

Buchsbaum, B.R., Olsen, R.K., Koch, P., Berman, K.F., 2005a. Human dorsal and ventral auditory streams subserve rehearsal-based and echoic processes during verbal working memory. Neuron 48, 687–697.

Buchsbaum, B.R., Olsen, R.K., Koch, P.F., Kohn, P., Kippenhan, J.S., Berman, K.F., 2005b. Reading, hearing, and the planum temporale. NeuroImage 24, 444–454.

Burock, M.A., Dale, A.M., 2000. Estimation and detection of event-related fMRI signals with temporally correlated noise: a statistically efficient and unbiased approach. Hum. Brain Mapp. 11, 249–260.

Cowan, N., 1995. Attention and Memory: An Integrated Framework. Oxford University Press, New York.

Dale, A.M., Buckner, R.L., 1997. Selective averaging of rapidly presented individual trials using fMRI. Hum. Brain Mapp. 5, 329–340.

Derrfuss, J., Brass, M., von Cramon, D.Y., 2004. Cognitive control in the posterior frontolateral cortex: evidence from common activations in task coordination, interference control, and working memory. NeuroImage 23, 604–612.

Duncan, J., Owen, A.M., 2000. Common regions of the human frontal lobe recruited by diverse cognitive demands. Trends Neurosci. 23, 475–483.

Fox, M.D., Snyder, A.Z., Vincent, J.L., Corbetta, M., Van Essen, D.C., Raichle, M.E., 2005. The human brain is intrinsically organized into dynamic, anticorrelated functional networks. Proc. Natl. Acad. Sci. U. S. A. 102, 9673–9678.

Frith, C.D., Friston, K.J., Liddle, P.F., Frackowiak, R.S., 1991. A PET study of word finding. Neuropsychologia 29, 1137–1148.

Glover, G.H., 1999. Deconvolution of impulse response in event-related BOLD fMRI. NeuroImage 9, 416–429.

Hairston, W.D., Hodges, D.A., Casanova, R., Hayasaka, S., Kraft, R., Maldjian, J.A., Burdette, J.H., 2008. Closing the mind's eye: deactivation of visual cortex related to auditory task difficulty. Neuroreport 19, 151–154.

Henson, R., Rugg, M.D., Friston, K., 2001. The choice of basis functions in event-related fMRI. NeuroImage 13, s149.

Hunter, M.A., Takane, Y., 2002. Constrained principal component analysis: various applications. J. Educ. Behav. Stat. 27, 105–145.

Johnson, J.A., Zatorre, R.J., 2006. Neural substrates for dividing and focusing attention between simultaneous auditory and visual events. NeuroImage 31, 1673–1681.

Kahana, M.J., Sekuler, R., 2002. Recognizing spatial patterns: a noisy exemplar approach. Vis. Res. 42, 2177–2192.

Koenigs, M., Acheson, D.J., Barbey, A.K., Solomon, J., Postle, B.R., Grafman, J., 2011. Areas of left perisylvian cortex mediate auditory-verbal short-term memory. Neuropsychologia 49, 3612–3619.

Laurienti, P.J., Burdette, J.H., Wallace, M.T., Yen, Y.F., Field, A.S., Stein, B.E., 2002. Deactivation of sensory-specific cortex by cross-modal stimuli. J. Cogn. Neurosci. 14, 420–429.

Lewis-Peacock, J.A., Postle, B.R., 2008. Temporary activation of long-term memory supports working memory. J. Neurosci. 28, 8765–8771.

Lewis-Peacock, J.A., Postle, B.R., 2012. Decoding the internal focus of attention. Neuropsychologia 50, 470–478.

Manoach, D.S., Greve, D.N., Lindgren, K.A., Dale, A.M., 2003. Identifying regional activity associated with temporally separated components of working memory using event-related functional MRI. NeuroImage 20, 1670–1684.

Metzak, P.D., Feredoes, E., Takane, Y., Wang, L., Weinstein, S., Cairo, T., Ngan, E.T.C., Woodward, T.S., 2011. Constrained principal component analysis reveals functionally connected load-dependent networks involved in multiple stages of working memory. Hum. Brain Mapp. 32, 856–871.

Metzak, P.D., Riley, J., Wang, L., Whitman, J.C., Ngan, E.T.C., Woodward, T.S., 2012. Decreased efficiency of task-positive and task-negative networks during working memory in schizophrenia. Schizophr. Bull. 38, 803–813.

Oberauer, K., 2002. Access to information in working memory: exploring the focus of attention. J. Exp. Psychol. Learn. Mem. Cogn. 28, 411–421.

Oztekin, I., McElree, B., Staresina, B.P., Davachi, L., 2009. Working memory retrieval: contributions of the left prefrontal cortex, the left posterior parietal cortex, and the hippocampus. J. Cogn. Neurosci. 21, 581–593.

Oztekin, I., Davachi, L., McElree, B., 2010. Are representations in working memory distinct from representations in long-term memory? Neural evidence in support of a single store. Psychol. Sci. 21, 1123–1133.

Postle, B.R., 2006. Working memory as an emergent property of the mind and brain. Neuroscience 139, 23–38.

Price, C.J., Crinion, J.T., Macsweeney, M., 2011. A generative model of speech production in Broca's and Wernicke's areas. Front. Psychol. 2, 237.

Raichle, M.E., MacLeod, A.M., Snyder, A.Z., Powers, W.J., Gusnard, D.A., Shulman, G.L., 2001. A default mode of brain function. Proc. Natl. Acad. Sci. U. S. A. 98, 676–682.

Ranganath, C., Cohen, M.X., Dam, C., D'Esposito, M., 2004. Inferior temporal, prefrontal, and hippocampal contributions to visual working memory maintenance and associative memory retrieval. J. Neurosci. 24, 3917–3925.

Rapin, L., Loevenbruck, H., Dohen, M., Metzak, P.D., Whitman, J.C., Woodward, T.S., 2012. Hyperintensity of functional networks involving voice-selective cortical regions during silent thought in schizophrenia. Psychiatry Res. Neuroimaging 202, 110–117.

Riecker, A., Mathiak, K., Wildgruber, D., Erb, M., Hertrich, I., Grodd, W., Ackermann, H., 2005. fMRI reveals two distinct cerebral networks subserving speech motor control. Neurology 64, 700–706.

Rottschy, C., Langner, R., Dogan, I., Laird, A.R., Schulz, J.B., Fox, P.T., Eickhoff, S.B., 2012. Modelling neural correlates of working memory: a coordinate-based meta-analysis. NeuroImage 60, 830–846.
Serences, J.T., 2004. A comparison of methods for characterizing the event-related BOLD timeseries in rapid fMRI. NeuroImage 21, 1690–1700.
Shulman, G.L., Corbetta, M., Buckner, R.L., Raichle, M.E., Fiez, J.A., Miezin, F.M., Petersen, S.E., 1997. Top-down modulation of early sensory cortex. Cereb. Cortex 7, 193–206.
Sternberg, S., 1966. High-speed scanning in human memory. Science 153, 652–654.
Takane, Y., Hunter, M.A., 2001. Constrained principal component analysis: a comprehensive theory. AAECC 12, 391–419.
Takane, Y., Shibayama, T., 1991. Principal component analysis with external information on both subjects and variables. Psychometrika 56, 97–120.
Vinckier, F., Dehaene, S., Jobert, A., Dubus, J.P., Sigman, M., Cohen, L., 2007. Hierarchical coding of letter strings in the ventral stream: dissecting the inner organization of the visual word-form system. Neuron 55, 143–156.
Woodward, T.S., Cairo, T.A., Ruff, C.C., Takane, Y., Hunter, M.A., Ngan, E.T.C., 2006. Functional connectivity reveals load dependent neural systems underlying encoding and maintenance in verbal working memory. Neuroscience 139, 317–325.
Zatorre, R.J., 2007. There's more to auditory cortex than meets the ear. Hear. Res. 229, 24–30.